

REVIEW ARTICLE OPEN

Physics and applications of charged domain walls

Petr S. Bednyakov¹, Boris I. Sturman², Tomas Sluka³, Alexander K. Tagantsev^{4,5} and Petr V. Yudin¹

The charged domain wall is an ultrathin (typically nanosized) interface between two domains; it carries bound charge owing to a change of normal component of spontaneous polarization on crossing the wall. In contrast to hetero-interfaces between different materials, charged domain walls (CDWs) can be created, displaced, erased, and recreated again in the bulk of a material. Screening of the bound charge with free carriers is often necessary for stability of CDWs, which can result in giant two-dimensional conductivity along the wall. Usually in nominally insulating ferroelectrics, the concentration of free carriers at the walls can approach metallic values. Thus, CDWs can be viewed as ultrathin reconfigurable strongly conductive sheets embedded into the bulk of an insulating material. This feature is highly attractive for future nanoelectronics. The last decade was marked by a surge of research interest in CDWs. It resulted in numerous breakthroughs in controllable and reproducible fabrication of CDWs in different materials, in investigation of CDW properties and charge compensation mechanisms, in discovery of light-induced effects, and, finally, in detection of giant two-dimensional conductivity. The present review is aiming at a concise presentation of the main physical ideas behind CDWs and a brief overview of the most important theoretical and experimental findings in the field.

npj Computational Materials (2018)4:65; doi:10.1038/s41524-018-0121-8

INTRODUCTION

Ferroelectric materials are very often split into domains, areas that differ in the direction of spontaneous polarization.^{1,2} Domain walls (DW)—very thin regions separating domains—play an essential role in the electrical, electromechanical, and optical properties of ferroelectrics. For example, a high wall mobility promotes fast polarization switching of the material.³ Until recently, although the structure of ferroelectric walls was addressed both in theory and experiment, researchers mainly cared about ferroelectric walls as borders between adjacent domains, rather than finite-thickness areas exhibiting certain internal structure. However, with a shift of the researchers' attention from the micron to nanometer scale, one got interested in the "inner" properties of ferroelectric and, in general, ferroic DWs. Specifically, DWs were considered in the context of nanoelectronics.⁴

One of the "inner" properties of ferroic walls is their ability to carry some bound charge, which is apt to be screened with free carriers. Walls carrying bound charge are termed charged domain walls (CDWs). Remarkably, the screening takes place even in the case where the adjacent domains are insulating.⁵ Keeping in mind that the walls are often easily movable, CDWs can be viewed as ultrathin movable conductive sheets embedded into an insulating material.

The pursuit of nano-electronic applications motivated CDW studies in the 21st century. CDWs have been documented in many ferroelectrics, including perovskite and non-perovskite oxide materials, polymer compositions, and improper ferroelectrics. A conductivity wall/domain contrast up to 13 orders of magnitude has been recently reported.⁶ A number of methods enabling CDW engineering have been developed, and first device prototypes exploiting CDWs appeared.^{7,8}

Various CDW issues were reviewed in refs^{9–11}. Not competing with these articles, in the present paper, we are aiming at a synoptic presentation of the main concepts behind the understanding of CDWs, combined with a brief and updated review of important findings in the field.

BASIC INFORMATION ABOUT CDWS

For two adjacent domains 1 and 2 with polarizations \mathbf{P}_1 and \mathbf{P}_2 , the bound charge with the surface density

$$\sigma_p = (\mathbf{P}_2 - \mathbf{P}_1) \cdot \mathbf{n}_1, \quad (1)$$

is present at the wall separating them. Here \mathbf{n}_1 is the wall normal unit vector pointing inside domain 1. Since the bound charge creates electrostatic fields in the domains, which is energetically costly, DWs do not carry often any bound charge. Such walls are called neutral domain walls (NDWs). DWs with non-zero bound charge σ_p are called CDWs. The head-to-head (H-H) configuration in adjacent domains leads to a positive charge (Fig. 1a, b, d). Tail-to-tail (T-T) CDWs (with reversed arrows in Fig. 1a, b, d) are charged negatively. The head-to-tail walls, illustrated by Fig. 1c, can also carry bound charge; its sign depends on the wall orientation.

The presence of bound charge leads generally to its screening with free charges—electrons, holes, and/or mobile ions. This screening can be regarded as a distinctive feature of CDWs. It is useful often to distinguish two types of CDWs: strongly charged (SCDWs) and weakly charged (WCDWs). SCDWs cannot exist without charge screening because the electric field of the bound charge would destabilize ferroelectricity. WCDWs might exist as stable objects without charge screening, though the latter is very

¹Institute of Physics, Czech Academy of Sciences, Na Slovance 2, 18221 Prague 8, Czech Republic; ²Institute of Automation and Electrometry SB RAS, Koptuyg ave. 1, Novosibirsk 630090, Russia; ³CREAL3D SA, Chemin du Paqueret 1 A, CH-1025 Saint-Sulpice, Switzerland; ⁴Swiss Federal Institute of Technology (EPFL), CH-1015 Lausanne, Switzerland and

⁵Ioffe Institute, 194021 St. Petersburg, Russia

Correspondence: Petr V. Yudin (yudin@fzu.cz)

Received: 30 May 2018 Accepted: 2 November 2018

Published online: 30 November 2018

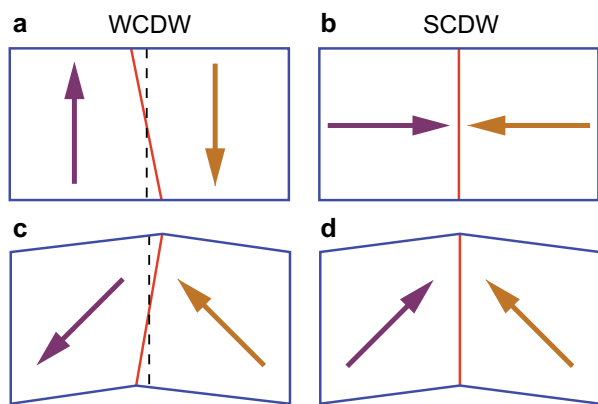


Fig. 1 Schematic of charged domain walls for tetragonal perovskite ferroelectrics. Arrows show directions of spontaneous polarization. **a** 180° non-ferroelastic weakly charged domain wall (WCDW). **b** 180° non-ferroelastic strongly charged domain wall (SCDW). **c** 90° ferroelastic WCDW. **d** 90° ferroelastic SCDW. Small deviations of WCDWs from their electro-neutral orientations (shown with dashed lines) are exaggerated. Twist in (c) and (d) schematically shows the difference in spontaneous strains between ferroelastic domains

likely. In the cases when the difference between SCDWs and WCDWs is not crucial, we will use the general abbreviation CDWs.

DWs slightly deviating from the electro-neutral orientations are typically WCDWs. They are illustrated by Fig. 1a, c. DWs in improper ferroelectrics, where the spontaneous polarization P_0 is not the order parameter, belong to WCDWs irrespectively of the orientation. Here, the electric field cannot destabilize ferroelectricity, it only reduces the value of P_0 .^{3,12,13} DWs in recently introduced hyperferroelectrics^{14–16} can also be regarded as WCDWs. Remarkably, NDWs can carry a distribution of the bound charge, while the total charge is zero.^{17,18}

In typical and most important proper oxide ferroelectrics, CDWs essentially deviating from the electro-neutral orientation are SCDWs. This case is illustrated by Fig. 1b, d. In such materials, the stabilization of SCDWs requires almost complete screening of the bound charge with free charges.¹³ This fact is of prime importance for the studies and practical harnessing of SCDWs.

It is also useful to distinguish the situations where the walls are ferroelastic (the adjacent domains differ in the spontaneous strain) and non-ferroelastic (the spontaneous strains are the same). They are illustrated by Figs. 1c, d and 1a, b, respectively. Elastic forces prevent rotation of ferroelastic walls contributing to the CDW stability.¹⁹ Most of experimentally accessed SCDWs are ferroelastic.

CDW OBSERVATIONS

In view of the high energy of their formation, CDWs were only occasionally mentioned in the past.^{20–24} In the 2000's, research activity focused on oxide interfaces^{4,25} revived the interest in electronically compensated CDWs as potential hardware of reconfigurable conducting paths. To date, CDWs are documented in many ferroelectrics, using different experimental techniques. Below, we overview the accumulated experimental findings, highlighting the results promising for applications and/or essentially contributing to the physics of CDWs (see the section 'Theoretical insights into CDW properties').

Since the 1980s, transmission electron microscopy (TEM) techniques has allowed experimentalists to resolve the shapes of DWs and identify their charged parts. In particular, CDWs were observed in KNbO_3 crystals²⁶ and $\text{Pb}(\text{Zr,Ti})\text{O}_3$ (PZT) ceramics.²² Presently, high-resolution and scanning TEM techniques allow for observation of individual atomic displacements and, hence, give

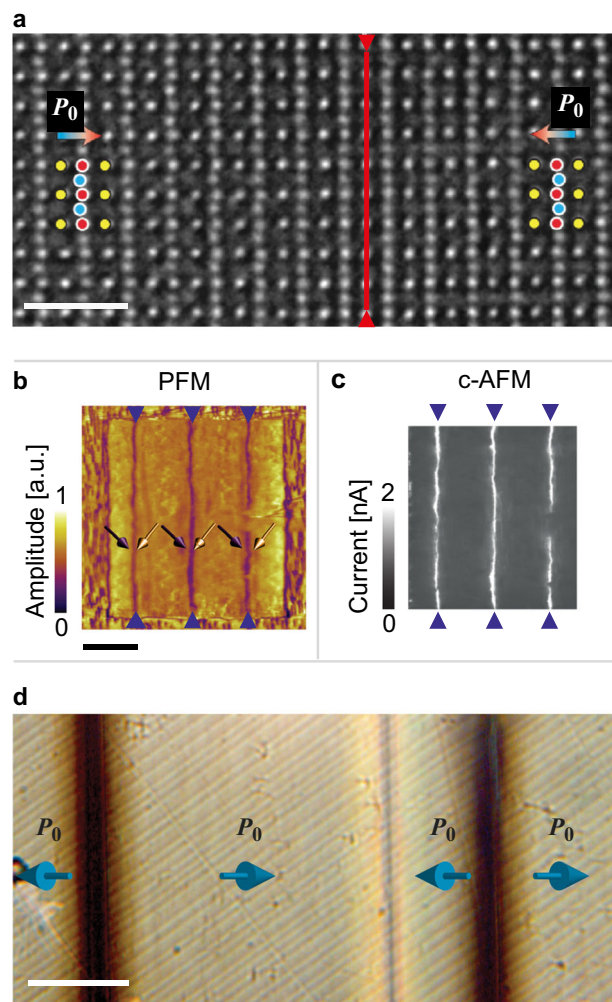


Fig. 2 Observation of ferroelectric CDWs. **a** High-resolution TEM image of a 180° CDW in ultra thin $\text{Pb}(\text{Zr}_{0.2}\text{Ti}_{0.8})\text{O}_3$ film, after ref.³⁵ (scale bar, 1 nm). This image enabled evaluation of a large thickness (5–10 nm) of the wall. Red line indicates the CDW center. **b, c** CDWs in La-modified BiFeO_3 thin films visualized via scanning probe microscopy. **b** Amplitude image of PFM signal in the vertical mode, which gives positions of the walls (scale bar, 1 μm). **c** Conductive-AFM image of the same area, after ref.⁴⁸. **d** 90° CDWs (vertical alternating dark and bright stripes) in $(110)_c$ oriented BaTiO_3 crystal observed with optical microscopy by an intensity analysis of transmitted non-polarized light (scale bar, 100 μm). The contrast is conditioned by the rotations of the optical indicatrices of ferroelastic domains. After ref.⁶⁸

information about the internal CDW structure. With these techniques, CDWs were documented in single crystals of LiNbO_3 ,²⁷ YMnO_3 ,²⁸ and $(\text{Ca,Sr})_3\text{Ti}_2\text{O}_7$,^{29,30} thin films of BiFeO_3 ,^{8,31–33} PbTiO_3 ,³⁴ and PZT,^{35–40} and ceramics of BiFeO_3 ,⁴¹ $(\text{K,Na})\text{NbO}_3$,⁴² TmMnO_3 ,⁴³ and LuMnO_3 .⁴³ TEM techniques, supplemented by analyses of the energy losses of electrons (EELS) were employed recently to detect elemental components of the material in the vicinity of CDWs.^{30,38–41} Other methods were also in use: scanning electron microscopy for observations of the intersections of CDWs with etched surfaces of LiNbO_3 crystals,⁴⁴ high-resolution X-ray photoemission electron microscopy to visualize and characterize conducting DWs in ErMnO_3 ,⁴⁵ low-energy electron microscopy (electron backscattering) to image CDWs in LiNbO_3 crystals.⁴⁶

High-resolution TEM studies have provided crucial information about the widths of domain walls. Figure 2a shows one of the images obtained in such studies. This image enabled evaluation of

the CDW thickness (5–10 nm) against (1–2 nm) for the NDW in PZT ultra thin films.³⁵ This experimental finding corroborates the theoretical insights and estimates and supports the approach currently used for the description of CDWs which are roughly one order of magnitude thicker than NDWs (see the section 'Theoretical insights into CDW properties').

Different variants of scanning probe microscopy were extensively used in the studies of CDWs on the mesoscale. A combination of piezo-force microscopy (PFM) with conductive atomic force microscopy (c-AFM) was found to be an efficient tool for CDW identification.⁴⁷ Using such an approach, CDWs in BiFeO₃:La thin films were documented.⁴⁸ Here, the information about the phase and amplitude of signals in the vertical and lateral modes enables one to locate the positions of CDWs. Figure 2b shows an amplitude image of PFM signal in the vertical mode. It gives the positions of the walls while they were identified as SCDWs, using the phase of this signal combined with the PFM signal in the lateral mode (not shown). An enhanced conduction of these walls was documented, using c-AFM (Fig. 2c). In combination and separately, PFM and c-AFM techniques were also applied for CDW observation in PZT,^{38,40,49,50} BiFeO₃,^{31,48,51} and PST⁵² thin films, ErMnO₃,^{53,54} LiNbO₃,^{55,56} HoMnO₃,⁵⁷ YbMnO₃,⁵⁸ and Cu₃B₇O₁₃Cl⁵⁹ crystals, BiFeO₃ ceramics,⁴¹ hybrid improper ferroelectric (Ca, Sr)₃Ti₂O₇,⁶⁰ and organic ferroelectrics.⁶¹

Other scanning techniques employed for CDW visualization are: Kelvin-probe force microscopy in HoMnO₃,⁵⁷ microwave impedance characterization in Pr(Sr_{0.1}Ca_{0.9})₂Mn₂O₇,⁶² scanning spreading resistance microscopy in BiFeO₃,⁸ and local Hall effect in YbMnO₃.⁵⁸

On the millimeter scale, CDWs can be detected optically in the reflection and transmission configurations. The first one is relevant to experiments with BaTiO₃ and PbTiO₃,²¹ LiNbO₃,^{24,63–66} and Pb₃Ge₃O₁₁.^{23,67} As for the transmission configuration, CDWs in (110)_c and (111)_c cuts of BaTiO₃ crystals (hereafter the subscript c indicates the pseudocubic reference frame) were observed both in polarized and non-polarized (Fig. 2d) light.^{13,68–72} Non-ferroelastic 180° CDWs were also identified in transmitted polarized light in PbTiO₃ and LiNbO₃ crystals.^{21,56,65}

CDWs were also observed, using other optical methods: The two-beam photorefractive coupling and directional light scattering in Sn₂P₂S₆,⁷³ surface laser intensity modulation in LiNbO₃,²⁴ second-harmonic generation in Pr(Sr_{0.15}Ca_{0.85})₂Mn₂O₇,⁷⁴ Cherenkov second-harmonic generation in LiNbO₃,^{75,76} Raman confocal microscopy in LiNbO₃, LiTaO₃, and SBN,^{77,78} and optical microscopy in LiNbO₃⁶⁶ and Pr(Sr_{0.15}Ca_{0.85})₂Mn₂O₇.⁷⁴ Raman scattering was also employed to determine the local symmetry in the vicinity of CDWs in LiNbO₃, LiTaO₃,^{77,78} BaTiO₃⁶⁹ and (K,Na)NbO₃.⁷⁹

THEORETICAL INSIGHTS INTO CDW PROPERTIES

Here, we overview the available theoretical knowledge on such important properties of CDWs as concentrations of screening charges, the wall thicknesses, and the formation energies. These properties and their interrelations will be considered mainly for SCDWs. Modeling of CDW conductivity is reviewed in the section 'CDW conductivity'.

For SCDWs with representative polarization $P_0 = 30 \mu\text{C}/\text{cm}^2$ and wall width $w = 10 \text{ nm}$,^{13,35,80} the screening charge concentration can be estimated as $2P_0/ew \approx 3 \times 10^{20} \text{ cm}^{-3}$, where e is the elementary charge. This is an extremely high value for nominally insulating wide-bandgap ferroelectrics. The screening charges can be electrons, holes, or/and mobile ions. For electron–hole (e–h) screening, high concentrations caused by band bending at the wall usually results in degeneracy of the fermion gas.⁸¹

For e–h screened SCDWs in typical proper ferroelectrics, the wall widths are expected to be appreciably larger than those in the case of NDWs. Along with the gradient energy in Landau theory,⁸² which promotes widening of DWs, for SCDWs, there

exists an additional widening mechanism.^{80,83} It is conditioned by a decreasing dependence of the kinetic energy⁸¹ of free electron (hole) gas on DW thickness w . This widening mechanism is found to be strong, leading roughly to about an order-of-magnitude increase of the SCDW width compared to that relevant to NDWs.^{80,83,84} This result was obtained with different calculation methods for 180° SCDWs within the Landau theory coupled to the quasi-classical Thomas–Fermi model⁸⁵ for the free-charge concentration. It was also shown that in the morphotropic boundary type materials (e.g., BaTiO₃ at room temperature), 90° SCDWs are expected to be yet a few times thicker than 180° SCDWs.⁸⁶ This is due to reduction of the excess order-parameter energy, owing to electron screening. The above estimate for 180° SCDWs corroborates the results of the comparative high-resolution TEM studies of NDW and SCDW in PZT (see the section 'CDW observations').

A more advanced treatment of 180° SCDWs was offered by combining the Landau theory with the self-consistent Hartree approximation for screening electrons.⁸⁷ It has revealed a generic discrete quantum structure of CDWs and the condition for employment of the Thomas–Fermi approximation. Specifically, the electron motion perpendicular to the walls is quantized such that the electron energy spectrum exhibits a finite number of subbands related to free electron propagation along the wall (Fig. 3a). This spectrum can cause specific light absorption associated with CDWs. It was shown also that the Thomas–Fermi approximation holds true when more than three electronic subbands are present. This is the case for typical oxide ferroelectrics. The true quantum screening regime with less than four electronic subbands looks interesting but exotic nowadays.

The above considerations imply that the ferroelectric possesses electronic states only below the valence band (VB) edge E_V and above the conductive band (CB) edge E_C . However, any real material possesses localized electronic levels (traps) within the bandgap. Experiments show that the effective trap concentration N_t varies around 10^{17} cm^{-3} in nominally undoped ferroelectrics.⁸⁸ It was shown analytically and numerically^{84,87} that the presence of traps leads to modification of the SCDW structure: The wall consists of a relatively narrow core, containing most of the screening charge, and some tails (Fig. 3b) so that the potential decays far from the core. The width of the core is close to the wall width w , obtained with neglected traps,^{80,87} while the tail length l is much larger than w . For a H–H CDW (electron screening), the most important parameters—the width w_e , the tail length l_e , and

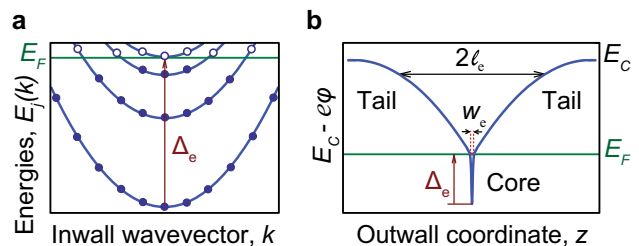


Fig. 3 General quantum and spatial properties of CDWs. **a** Schematic electronic structure of the wall, E_F is the Fermi energy, $E_j(k)$ is the dependence of the electron energy on the inwall wavevector for the j -th subband, and Δ_e is the difference between the energy at the wall center and the Fermi level (the core energy drop). The levels with energies $E_j(k) \lesssim E_F$ are filled with electrons. **b** Schematic band-bending diagram showing position of the CB edge in the presence of electrostatic potential ϕ for a 180° CDW of the H–H type. The spatial structure of the wall includes the core and tails; w_e is the CDW width, l_e is the tail length, and E_C refers to the case $\phi = 0$. After ref.⁸⁷

the core energy drop Δ_e (Fig. 3b)—are found to be^{80,87}

$$\begin{aligned} w_e &\simeq 1.3(\hbar^6 \varepsilon_f^3 / P_0 m_e^3 e^5)^{1/5} \\ \ell_e &\simeq 0.4 \sqrt{\varepsilon_f (E_C - E_F) / e^2 N_t} \\ \Delta_e &\simeq 4.35(\hbar^6 P_0^4 / \varepsilon_f^2 m_e^3)^{1/5}, \end{aligned} \quad (2)$$

where $\varepsilon_f \gg 1$ is the dielectric constant, m_e is the effective electron mass, and E_F is the Fermi energy. The condition of degeneracy of electrons is $k_B T \ll \Delta_e$. For a T–T CDW, it is sufficient to replace m_e by the hole mass m_h and $E_C - E_F$ by $E_F - E_V$. For representative parameters $P_0 = 30 \mu\text{C}/\text{cm}^2$, $\varepsilon_f = 500$, $m_e/m_e^0 = 0.3$ (m_e^0 is the free electron mass), $N_t = 10^{17} \text{cm}^{-3}$, and $E_C - E_F = 1.5 \text{eV}$ we obtain: $w_e \simeq 7 \text{nm}$, $\ell_e \simeq 1 \mu\text{m}$, and $\Delta_e \simeq 0.4 \text{eV}$. These rough estimates also show that the SCDW width w exceeds the width of NDWs by nearly one order of magnitude. The theoretical prediction of the tails has yet to be verified in an experiment.

The formation energy is a vital characteristic of CDWs, for it controls the possibility of their spontaneous appearance and deliberate creation of them. For typical proper oxide ferroelectric treated as a defect-free dielectric, the formation energy (per unit area) of an individual electron (or hole) screened SCDW in an isolated sample can be estimated⁸⁰ as $W \simeq 2P_0 E_g / e$ whereas $E_g = E_C - E_V$ is the bandgap. The same estimate is valid for creation of a couple of walls: electron screened SCDW + hole screened SCDW. This estimate has a simple interpretation: for the full screening, one should transfer $2P_0/e$ electrons [per unit area] across the bandgap, paying the energy penalty E_g/e per electron. A more elaborate treatment⁸⁷ provides expressions for the formation energies for the electron (W_e) and hole (W_h) screened CDWs:

$$W_e \simeq 2P_0(E_C - E_F)/e, \quad W_h \simeq 2P_0(E_F - E_V)/e. \quad (3)$$

Note that $W_e + W_h = W$. Since the electronic energies entering these expressions are $\simeq 1 \text{eV}$, these values are roughly two orders of magnitude larger than the typical NDW energies.⁸⁰ The above large formation energy rises a questions about feasibility of CDWs. Experimental observations of CDWs motivate one to look for energetically less costly screening scenarios, avoiding the electron transfer across the bandgap.

A possibility of reduction of CDW energy occurs if defects providing free carriers are *mobile*. Specifically, in n-type materials, electrons needed for screening of the bound charge at H–H CDWs can be collected from a macroscopically large area avoiding the electron transfer across the bandgap.¹³ At the same time, the ionized donors can be used for screening of T–T CDWs. Evidently, an analogous scenario works for p-type materials. In such “mixed” free-carrier/ion screening scenarios, substantially smaller wall-formation energies than for the e–h screening are expected.^{13,89} These screening scenarios entail a clear manifestation. In the case of a quasi-periodic H–H/T–T CDW pattern, the minimal possible period is expected to be a decreasing function of concentration of the defects providing free carriers. This prediction corresponds to the experimental data obtained for CDW structures in BaTiO_3 crystals possessing variable concentration of oxygen donor-like vacancies^{13,68} (see also the section ‘CDW engineering’).

An alternative way to avoid the over-bandgap electron transfer is to use super-bandgap illumination as a mean to produce screening electrons and holes. A theory of this mechanism of SCDW formation was recently offered.⁹⁰ It can be considered as a generalization of the previous results,^{80,87} which explores the concept of intensity-dependent quasi-Fermi levels for electrons and holes.⁹¹ This scenario has been implemented experimentally.⁷²

Above we restricted ourselves to infinite one-dimensional CDWs. What happens if a CDW connects two electrodes? This

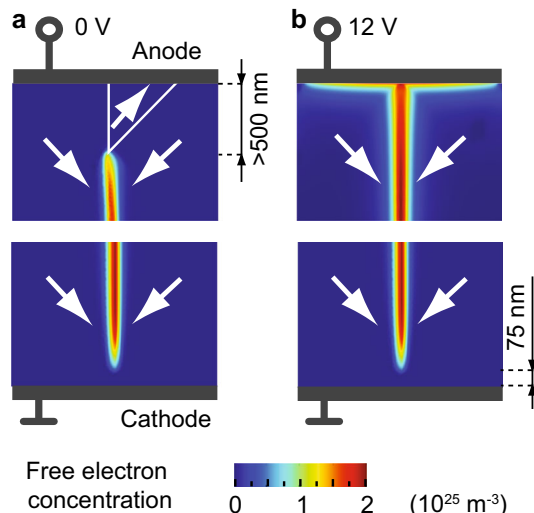


Fig. 4 Color-scale maps of the phase-field calculated free-electron concentration at a H–H CDW in BaTiO_3 contacted with an electrode.⁶⁸ **a** Short-circuited configuration, the electron gas is disconnected from both electrodes with dielectric gaps. **b** Under applied voltage of 12 V, one of the gaps is closed while the other becomes much narrower, facilitating electron tunneling. After ref.⁶⁸

brings us to a qualitatively different 2D case, which is relevant not only to the basics, but also to the conductivity issues to be considered in the section ‘CDW conductivity’. The matter is that the application of an equipotential electrode to the crystal surface flattens the band bending (Fig. 3b) in the vicinity of the electrode. On the other hand, this bending is the driving force for the free-charge accumulation at the wall.⁶⁸ Thus, the electron (hole) gas at CDWs can be *disconnected* from the electrodes with dielectric gaps. However these gaps can be essentially narrowed or even closed in the presence of a d.c. electric field. This is illustrated by Fig. 4 obtained by phase-field modeling.⁶⁸ In addition, the d.c. field can facilitate tunneling through the gaps.

The above discussion was dealing with theoretical insights into SCDWs. As for WCDWs, most attention was paid to improper ferroelectrics of the hexagonal manganite type, like ErMnO_3 . The wall structure was probed using the Landau theory⁹² in combination with ab initio calculations⁹³ while the effect of screening charge was ignored. The experimental profiles for NDWs and CDWs in ErMnO_3 ⁹² were approximated using the phenomenological model⁹² while the documented small differences between the thicknesses of NDWs and CDWs was attributed to the effect of the crystalline anisotropy.

Ab initio calculations within the density-functional theory (DFT) for CDWs is a less developed but rapidly growing activity. Most of DFT calculations are relevant to NDWs, see, e.g., refs^{47,94,95}. DFT simulations of CDWs represent a more complicated problem owing to the necessity to account for long-range correlation effects and trap recharging. Ab initio calculations⁵³ were performed for a 10-unit-cell stack of YMnO_3 , which contains one H–H and one T–T wall. In these materials, $P_0 \sim 6 \mu\text{C}/\text{cm}^2$, which, taking the wall width $w = 10 \text{nm}$,⁹² leads to a still appreciable bound charge concentration of $2P_0/ew \approx 0.6 \times 10^{20} \text{cm}^{-3}$. If this charge is screened with the e–h free carriers, to provide such screening, the Fermi level at the CDW should be quite close to the edge of the VB (or CB). This was observed in ab initio simulations,⁵³ where the Fermi level contacted VB. This should promote the conduction at T–T walls screened by holes, which is consistent with the experimental observations⁵³ (see the section ‘CDW conductivity’).

The advantage of ab initio simulations is a possibility of engineering of new materials. Recently, a concept of

hyperferroelectrics—a new class of proper ferroelectrics which are not destabilized by unscreened depolarization field was introduced.¹⁴ The possible CDWs in these materials may be naturally stable, as confirmed by first-principles calculations of H–H and T–T walls in ABC-type hexagonal hyperferroelectrics.¹⁶ However, scarce data on CDWs in hyperferroelectrics still need additional validation. Ab initio simulations are efficiently employed for bandgap design: the impact of CDWs on the bandgap width was addressed in organometal halide perovskites, which is of interest in the context of photovoltaics.⁹⁶

It should be mentioned that, for a CDW, besides the formation energy its stability is important. As was mentioned in the section 'Basic information about CDWs', elastic effects contribute to stability of ferroelastic CDWs. At the same time, even being screened, CDWs exhibit positive formation energy. This means that, unless the boundary conditions prevent disappearance of the walls, any CDW configuration has to be regarded as metastable. The decay mechanisms can be very complicated. In practice, depending on the type of ferroelectric, the temperature, etc., the decay time can range from a fraction of second to years.

CDW CONDUCTIVITY

The very large conductivity of CDWs in nominally insulating ferroelectrics is relevant both to the fundamental knowledge and applications in nanoelectronics.^{4,47,68} Here we represent first the main theoretical insights into CDW conduction properties and consider then the relevant experimental data.

In the case of e–h screening, CDW conductivity is expected to be due to the freedom of movement of the compensating electrons or holes in the wall plane. Since the concentrations of compensating free carriers at CDWs can readily be above 10^{20} cm^{-3} , large metallic-like inwall conductivity is expected. This simple idea, expressed in 1973,⁵ lies in the basis of all available models of CDW conductivity. In the case of mixed electron-ion screening, the ion-screened CDW is expected to possess a relatively small conductivity because of low ion mobility.

Let $n = n(z)$ be the concentration of the compensating charge carriers (electrons or holes) for positively or negatively charged walls as a function the coordinate z in the direction perpendicular to the wall. The specific bulk conductivity σ can be expressed as $\sigma = e\mu n$, where μ is mobility of the screening carriers. It is implied that the current flows along the wall, i.e., we deal with a quasi-2D effect. The specific surface CDW conductivity reads $\sigma_s = e\mu\bar{n}w$, where \bar{n} is the average over z concentration of compensating carriers and w is the CDW width.

Determination of $n(z)$ and w requires modeling of CDW structure. In practice, inclined 180° CDWs, characterized by the inclination angle θ_i between the wall plane and the polarization direction, see Fig. 1a, b, are important. The total bound charge to be screened is $2P_0\sin\theta_i$ in this case, and the width w is expected to be weakly dependent on θ_i for not very small inclination angles. Thus, we have roughly $\bar{n}w \approx 2P_0\sin\theta_i$. This feature is consistent with the results of continuum numerical simulations for LiNbO_3 crystals.^{84,97}

This above continuum medium model of CDW conductivity is oversimplified. First, we know that the discrete quantum subband structure depicted in Fig. 3a is generic for CDWs. A part of the subbands can be filled with electrons (holes) and, thus, excluded from the charge transport. For this reason, the total concentration of conductive charge carriers can be substantially smaller than $2P_0\sin\theta_i$. This can explain the results of recent experiments with CDWs in YbMnO_3 crystals.⁵⁸ Second, the mobility μ can differ substantially from the value expected for the 3D band transport in metals. This can be due to (i) roughness of the CDW and (ii) 2D character of the electron scattering processes.

Often, CDW conduction experiments run in tip configurations when the electric current flows between a continuous bottom

electrode and a tip top electrode. Here, the total resistance extracted from the I – V characteristic can be approximated by $R = F/\sigma_s$ where $F \approx 0.72 \log(5d/a)$ is a dimensionless geometric factor accounting for a sharp convergence of stream lines of the current density from continuous bottom electrode to the tip.⁶ Fortunately, it depends weakly on the ratio of the sample thickness d to the tip contact length a facilitating estimates of σ_s and σ from experimental data.

The presence of a large CDW conductivity does not ensure that it is easily available via Ohmic contacts. As we have seen in the section 'Theoretical insights into CDW properties', dielectric gaps are possible between the electrodes and highly conductive electron gas at the wall. These gaps depend generally on the applied d.c. voltage V and the work-function difference between the crystal and metal. Thus, complicated I – V characteristics are generally envisaged.

Turning to the experimental side, we mention first that an elevated conductivity of SbSI crystals owing to the presence of CDWs was reported already in 1976.²⁰ At that time, it did not attract a strong interest. Such an interest arose in 2009 after the report of high local conductivity of domain walls in BiFeO_3 crystals.^{47,98} However, the walls investigated were nominally neutral. A stimulating result, relevant to CDWs, dates from 2012 when a large conductivity was detected at transient CDWs of nucleating nano-domains in PZT thin films.⁵⁰ The conductivity contrast between the walls and the bulk reached $\sim 10^4$. This discovery triggered a research endeavor to detect and explore similar phenomena in other systems.

An important advance was achieved with 90° CDWs in BaTiO_3 stabilized by the ferroelastic clamping.⁶⁸ Experiments were conducted with a set of pad electrodes covering either H–H, or T–T CDWs, or bulk areas (Fig. 5a). Conductivity of the T–T CDWs

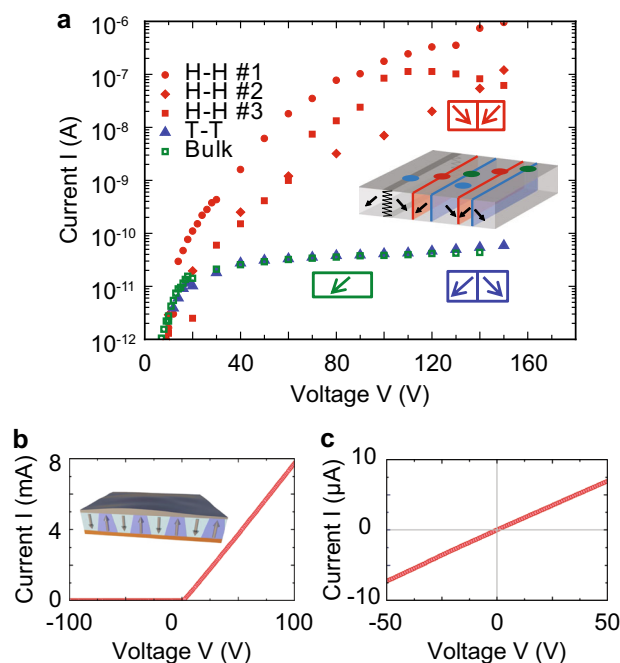


Fig. 5 CDW conductance in BaTiO_3 **a** and LiNbO_3 **b**, **c** crystals. **a** I – V characteristic for different regions of the crystal: with a H–H SCDW, with a T–T CDW, and without walls. Insert shows schematically the experimental configuration comprising $\langle 110 \rangle_c$ oriented BaTiO_3 crystal with CDWs; top pad electrodes (Pt) are shown with circles while the continuous bottom electrode is not shown. After ref. ⁶⁸. **b**, **c** I – V characteristics for different CDW configurations in LiNbO_3 : an array of 1464 parallel CDWs sandwiched between top (Ag) and bottom (Cr) electrodes **b** and an array of 32 parallel CDWs contacted by two Cr pads patterned from the bottom electrode **c**. After ref. ⁶

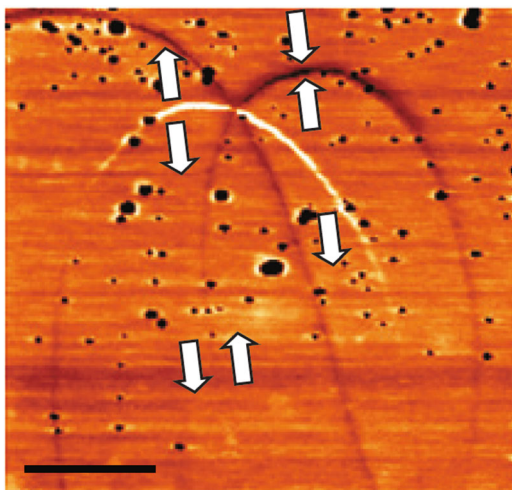


Fig. 6 CDW conductance in improper ferroelectric ErMnO₃. The c-AFM scan shows suppressed conductance at H–H walls (dark), enhanced conductance at T–T walls (bright), and a continuous transition between these two states with changing inclination angle (scale bar, 2 μm). Arrows show the direction of \mathbf{P}_0 . After ref. ⁵³

showed no difference compared to the bulk. However, conductivity of the H–H CDWs was found to be much higher than that of the bulk. This is illustrated by Fig. 5a. Using the data of Fig. 5a, the conductivity of the H–H CDWs was evaluated to be 10^8 – 10^{10} times higher than that of the bulk. Furthermore, this conductivity exhibited a metallic-type decreasing temperature dependence. A remarkable feature of this CDW conductivity was the threshold behavior of the I – V dependence (see the section ‘Theoretical insights into CDW properties’). Such a behavior is explained within the CDW theory. The absence of large conductivity at T–T CDWs is in agreement with the electron/ion screening scenario for CDWs in BaTiO₃: the H–H CDWs are screened by highly mobile electrons while T–T walls are screened by much less mobile oxygen vacancies (see the section ‘Theoretical insights into CDW properties’).

Using the c-AFM method, CDW conductivity was also detected in BiFeO₃ thin films.⁴⁸ The current flowing through H–H CDWs was more than three orders of magnitude larger than that flowing through the bulk or through NDWs. Figure 2b, c show a PFM image of the domain structure and the corresponding map of electric current. Conducting lines are clearly seen at H–H CDWs. The H–H CDWs exhibited a non-thermally-activated conductivity, which contrasted with a thermally-activated conductivity of 71° nominally neutral walls.

Ferroelastic bent CDWs in PZT also exhibit non-thermally-activated conductivity. Narrow ferroelastic domain inclusions limited with a pair of weakly bent ferroelectric walls were addressed. In view of their weak bending, the walls are expected to be WCDWs. Using high-resolution cryogenic c-AFM, clear current maxima corresponding to each of the two bent DWs limiting narrow inclusions were identified.³⁸ Also, a correlation between the local concentration of charged dopants and the CDW conductance was established using the EELS TEM technique.⁴⁰

In 2017, record-breaking conductivity was reported for 180° CDWs in LiNbO₃ crystals,^{6,7,6,99} while the earlier studies reported only transient currents⁶⁶ and d.c. conductivity under super-bandgap illumination.⁵⁵ We highlight here the results from ref. ⁶. In this work, inclined ($\theta_i \approx 1^\circ$) positively charged walls (and also arrays of such walls) were engineered, using biased μm -sized tips. Conductance was measured, using different configurations of electrodes made of different materials. The conductance of a wall array measured between a bottom Cr electrode and Ag-paste top electrode was reported to be of rectifying type (Fig. 5b). The

measurements where the wall was contacted with two bottom Cr electrodes yielded the ohmic behavior (Fig. 5c). The data of Fig. 5c were used to evaluate the specific surface resistance of CDWs and their bulk conductivity σ . With the wall width $w = 10$ nm, the latter was estimated as $\sigma \approx 0.02(\Omega\text{cm})^{-1}$. This value exceeds the dark conductivity of LiNbO₃ by at least 13 orders of magnitude. While the CDW thermally-activated conductivity was highly stable for $T \lesssim 70^\circ\text{C}$, it decayed gradually and irreversibly at higher temperatures. This can be interpreted by the replacement of the e–h screening with the ionic charge compensation via thermo-activated migration of charged defects.

CDW conductance in improper ferroelectrics drew considerable attention as well, hexagonal manganites were of prime interest here. In these materials, DWs are interlocked with structural antiphase boundaries resulting in a full spectrum of DW orientations, ranging from neutral to maximally charged. Figure 6 illustrates this situation for ErMnO₃ crystals.⁵³ As seen from conducting-AFM contrast in Fig. 6, CDWs in hexagonal manganites demonstrate both increased (T–T) and suppressed (H–H) conductivities. The enhanced conduction of T–T walls demonstrated in this figure is consistent with the results of ab initio calculations (see the section ‘Theoretical insights into CDW properties’). Similar conductive behavior was reported in hybrid improper ferroelectric Ca_{2.46}Sr_{0.54}Ti₂O₇.⁶⁰ Despite their suppressed conductivity at relatively low applied voltages, H–H CDWs can be switched into a conductive state when a threshold voltage is exceeded, as demonstrated for ErMnO₃.¹⁰⁰

Recently c-AFM conduction experiments were advanced to include local Hall measurements.⁵⁸ This was done as applied to T–T CDWs in YbMnO₃ crystals. The positive sign of screening charge carriers (holes) and their mobility $\mu \approx 50$ cm²/Vs, relevant to the band transport, were established. Remarkably, the estimated concentration of screening holes ($\sim 10^{16}$ cm^{−3}) was found to be about four orders of magnitude below the value of $2P_0/ew$ for $w = 10$ nm. This can be qualitatively interpreted as a manifestation of the quantum subband structure of the wall (see the section ‘Theoretical insights into CDW properties’).

CDW ENGINEERING

A lot of efforts were put into engineering of CDW patterns in the tetragonal phase of BaTiO₃ crystals.^{13,68,72} The basic method used was the frustative poling:^{13,101} a thin crystal plate is brought into the tetragonal phase under a dc electric field normal to it, which equally favors two or more tetragonal domain states. For the [110]_c oriented field, the preferable tetragonal states are poled along [010]_c and [100]_c directions, while, for the [111]_c orientation, the preferable states are poled along [010]_c, [100]_c, and [001]_c. Frustative poling not necessarily leads to CDW formation since NDWs with lower energy per unit area can be generated as well. To avoid the preference of the system to form NDWs, one should reduce the formation energy of CDWs in question.

Frustative poling was implemented on crossing the border to tetragonal ferroelectric phase from cubic or orthorhombic phases. Since the interphase borders on the field/temperature (E – T) diagram are inclined, they can be crossed either by variation of E (Fig. 7a, line 2) or T (Fig. 7a, lines 1 and 3).

In the case of $\langle 110 \rangle_c$ poling of nominally stoichiometric BaTiO₃ and the cubic/tetragonal border, the preferable domain states can be separated either with a NDW parallel to the plane of the plate or with a CDW normal to it. Though, the energy per unit area of NDWs is smaller than that of CDWs (see the section ‘Theoretical insights into CDW properties’), a smaller area of a CDW reduces the formation energy of the latter.

In ref. ¹³ for $\langle 111 \rangle_c$ poling (the (E – T) ‘trajectory’ is shown in Fig. 7a with line 3), the competing NDWs and CDWs had approximately the same areas. Nevertheless, CDW patterns were generated, by using samples with elevated oxygen deficiency,

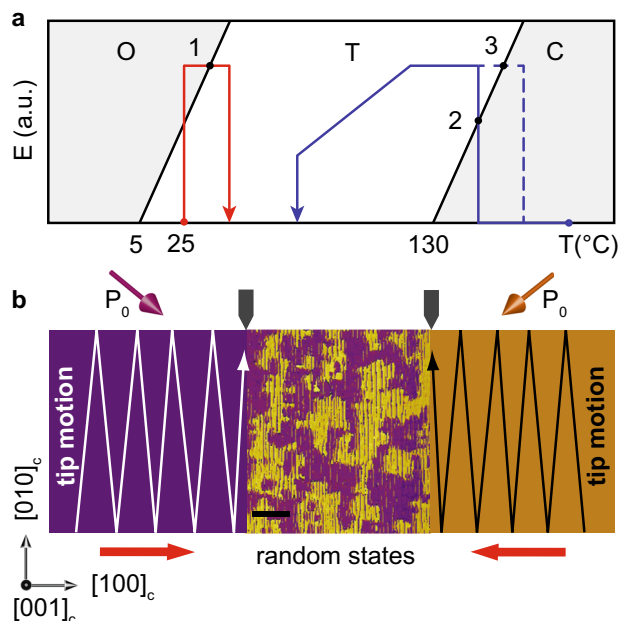


Fig. 7 Engineering of CDWs in BaTiO_3 crystals and BiFeO_3 films. **a** Schematic field/temperature (E - T) phase diagram of BaTiO_3 for $\langle 111 \rangle_c$ or $\langle 011 \rangle_c$ orientations of frusative field. The borders between the cubic (C), tetragonal (T), and orthorhombic (O) phases are shown with straight lines. Lines (with arrows) 1, 2, and 3 show sequence of changes of E and T used for engineering of 90° CDWs in refs ^{13,68,72}, respectively. **b** Engineering of CDWs in $[001]_c$ films of $\text{BiFeO}_3:\text{La}$ using trailing field.¹⁰² The map of sign of $[100]_c$ component of the spontaneous polarization (dark—positive, bright—negative). The as-grown film exhibits random domain states (scale bar, $1\ \mu\text{m}$). The right and left parts of the film are treated with a biased AFM tip, moving along zig-zag lines. This creates an effective trailing field¹⁰² directed along red arrows. The vertical components of the field under the AFM tip combined with the effective trailing field brings the left and right parts of the film into single-domain states. The in-plane polarization components are shown with P_0 -marked arrows. Once two encountering domains (shown with homogeneous colors) merge, a CDW forms. After ref. ⁴⁸

proving the enhanced concentrations of free electrons and mobile donors (oxygen vacancies), which promote the mixed electron/ion screening scenario with essentially reduced CDW energy (see the section 'Theoretical insights into CDW properties'). A remarkable correlation between the charge concentration and the domain size was reported, which is consistent with the theoretical prediction for this scenario. Yet another approach to the reduction of the CDW formation energy was employed in ref. ⁷². Here, for $\langle 111 \rangle_c$ poling in nominally stoichiometric BaTiO_3 , the orthorhombic/tetragonal phase border was crossed along line 1 in Fig. 7a, under a super-bandgap illumination that reduces the CDW formation energy (see the section 'Theoretical insights into CDW properties'). One should note that the CDW patterns in $\langle 111 \rangle_c$ plates are always stable under a moderate electric field ($\sim 1\ \text{kV/mm}$), while after removal of the field the domain patterns may persist for a long time or disappear quickly, depending on the sample.

In the view of utilizing CDWs for nanocircuitry, CDW nanoscale manipulation in La-doped BiFeO_3 thin films is of special interest.⁴⁸ As-grown films exhibit a random mixture of domain states (central part of Fig. 7b). The films were scanned with a biased AFM tip, which followed special trajectories creating an effective trailing field.¹⁰² Such a scanning leads to formation of two encountering domains (Fig. 7b). Merging the encountering domains yields a CDW.⁴⁸ In this approach, the tip-geometry-enhanced electron tunneling into the ferroelectric film was exploited to promote an

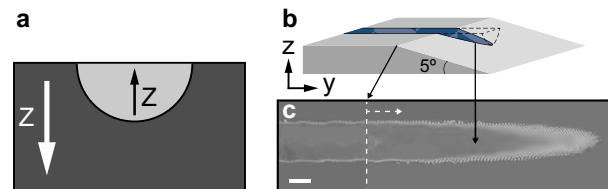


Fig. 8 Domain structure of a UV treated sample of LiNbO_3 after its subsequent repoling. **a** Schematic front view for created domain line. The inclination angle of CDW θ_i varies from 90° at the maximum depth to 0° at the surface. **b** Geometrical scheme of the repoled and then wedge polished sample. **c** Top view of the wedge polished and etched sample imaged with scanning electron microscopy (scale bar, $1\ \mu\text{m}$). After refs ^{108,111}

efficient screening of the bound charge and reduce the CDW formation energy. Some results of characterization of the CDW pattern created in this way are shown in Fig. 2b, c. This method was also applied to CDW engineering in $(\text{Pb,Sr})\text{TiO}_3$ thin films.⁵² In this work, along with the trailing electric field, the formation of CDWs was also controlled with poling using patterned electrodes.

Next we consider specific features of CDW engineering in LiNbO_3 . They are due to two interrelated factors—specific ferroelectric properties¹⁰³ and persistent experimental efforts toward optical applications.^{27,65,104,105} Domain walls in this material can be neutral, weakly, and strongly charged. Commercially available periodic domain structures, designed for optical applications, possess predominantly neutral or almost neutral DWs. However, there are numerous experimental tools for production of CDWs with a tunable angle θ_i between the wall and its electro-neutral orientation, which controls the bound charge.

Stable H-H CDWs with the inclination angle $\theta_i = 90^\circ$ were obtained first without application of electric fields by a severe heat-treatment close to the Curie temperature ($\approx 1200^\circ\text{C}$) with subsequent cooling down.¹⁰⁶ Field-assisted poling of commercially available z-cut LiNbO_3 wafers combining tip and continuous electrodes leads to inclined H-H CDWs with $\theta_i \approx 1^\circ$.^{6,55,76} The origin of the inclinations is not quite clear; most probably, they are due to expansion of the field stream lines toward the continuous electrode. The inclination angle can be varied by doping with Mg and thermal treatments.

A different method for fabrication of various domain structures leading to CDWs is known as prohibited poling.¹⁰⁷⁻¹¹¹ It can be exemplified as follows: a UV laser heats locally (on the μm scale) + z-face of a LiNbO_3 sample close to the Curie point. After cooling down, the sample shows no signs of domain inversion. However, during subsequent field-assisted repoling of the sample at room temperature, the exposed area remains non-inverted (prohibited poling), as shown schematically in Fig. 8a. The resulting domain structure possesses a CDW whose inclination angle θ_i varies from 90° at the maximum depth to 0° near the surface. Experimental evidences of such domain patterns are obtained by etching, PFM, and electron microscopy methods (Fig. 8b, c).

The physical mechanism behind the inhibition poling effect is, most probably, a local increase of the coercive field during the UV exposition because of high-temperature out-diffusion of lithium.¹⁰⁹ Remarkably, the CDW formation occurs pretty fast (on the scale of minutes), whereas diffusion of ions is extremely slow in lithium niobate.¹⁰³ This indicates that electrons are responsible for the charge screening.

Now we address CDW engineering in improper ferroelectrics. The available data suggest that spontaneous CDW formation^{53,59,60} occurs quite often. However, CDW engineering was only recently carried out in Cu-Cl boracite ferroelectrics.⁵⁹ In this material, the spontaneous polarization and spontaneous strain are linearly coupled. Exploiting this property of the material, quadrant domain structures were created with application of about 1 GPa

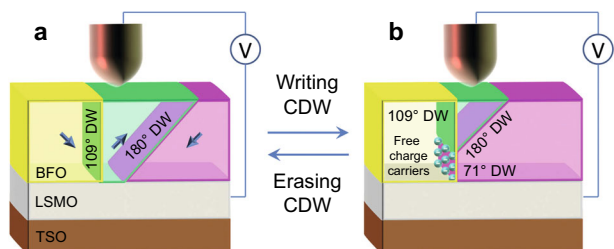


Fig. 9 Resistive switch using CDW in BiFeO₃ (BFO) film on TbScO₃ (TSO) substrate with (La,Sr)MnO₃ (LSMO) electrode. **a** Configuration containing only NDWs (109° DW and 180° DW). **b** Configuration containing also a segment CDW (71° DW). Both configurations are stable in absence of applied voltage. The configuration with a CDW segment is up to 10⁵ times more conductive than the other. By applying positive or negative voltage to the tip one can switch between two configurations thus providing the resistive switching with the “on/off” ratio up to 10⁵. After ref.⁸

pressure in the middle of the quadrant. The structure contained NDWs as well as H–H and T–T 90° CDWs, the T–T walls were found highly conductive. It was shown that this way injected CDWs can also be displaced by applying a properly oriented dc electric field.

CDW FUNCTIONALITIES

Harnessing CDWs in prototypes of electronic devices can be viewed as an ultimate practical goal of the scientific activity in the field. On the way toward applications, conductance control via unique properties of CDWs received appreciable attention.^{7,8,58,100,112–117} Below we consider simple examples of CDW exploitation.

Nanodevices could be designed such that the high conductivity of the wall could be created or erased on demand to provide resistive switching. Such an idea can be implemented either in the parallel-plate-capacitor configuration^{8,112} or coplanar capacitor configuration.⁷

With (110)_c oriented films, the coplanar capacitor configuration was chosen to provide up to 10³ on/off ratio.⁷ Here, in the on regime, the coplanar electrodes were connected with a wall that contained both neutral and charged segments. The resistance was determined by the neutral segments because of their relatively small conductivity. This prototype of nonvolatile ferroelectric domain wall memory was scalable to below 100 nm, exhibited excellent endurance and retention characteristics, and a multilevel data storage capacity. Thus, an important step toward integrated multi-terminal nanoscale DW devices was made. Employment of configurations with very low CDW resistance will enable one to proceed to much higher on/off ratios.

The functionality of the parallel-plate setup made of a (100) BiFeO₃ film was shown to be essentially controlled by the presence of a CDW.⁸ The schematic of such a setup is shown in Fig. 9.

Here the configuration shown in Fig. 9a does not contain CDWs. By applying positive voltage to this configuration one can generate a segment of CDW (Fig. 9b), the length of which increases as a function of voltage. After the voltage removal, the modified configuration stays unchanged while by applying a large enough negative voltage, the system is then brought back to the original configuration. Thus, the system exhibits a switching instability. If the CDW segment is large enough (more than 20% of the film thickness in this experiment), the across-the-film conduction of the two states differs up to 5 orders of magnitude. The elevated conduction of the “on” state is controlled by two factors: the high conductivity of the CDW segment and the conductivity of the 180° NDW, which is enhanced due to the

impact of the electrostatic potential created by the charge at the CDW segment.

Manipulation of charge transport in H–H CDWs in improper ferroelectrics like hexagonal manganites was also demonstrated. In semiconducting ErMnO₃, an electric-field control switching between resistive and conductive states was documented.¹⁰⁰ In YbMnO₃, the T–T CDW conductance was manipulated with external magnetic field.⁵⁸

The suppressed conductivity of some DW parts in hexagonal manganites is of interest in view of potential application for nano-capacitors, particularly in YMnO₃, where insulating CDWs had conductivity contrast up to 500 with respect to the bulk.¹¹³ Along with enhanced conductivity and other potential functionalities, CDW enhanced piezo-response was also actively analyzed.^{69–71,101,118–120}

SUMMARY AND OUTLOOK

The last decade was marked by a tremendous progress in investigation of ferroelectric CDWs. The field has evolved into a vast area of experimental and theoretical studies with promising results for applications. To date, CDWs have been documented in both bulk crystals and thin films. Numerous experimental techniques operating at the nanoscale were applied to (developed for) the fabrication and identification of various walls (weakly and strongly charged, inclined, etc.) and for analysis of their properties. Giant CDW conductivity, with up to 13 orders of magnitude enhancement as compared to the bulk, is now reliably detected for numerous materials. The possibilities of creation, displacement, and annihilation of CDWs, as well as a number of applications, have been demonstrated. An impressive amount of theoretical studies have been performed employing analytical and numerical studies within the Landau theory and also ab initio DFT simulations. It is possible now to judge about the charge screening mechanisms inherent in CDWs, about their widths (~10 nm), energy, quantum structure, the effect of light, etc.

Despite this impressive progress, the studies of CDWs are still at their infancy and it is too early to compare CDW functionalities with other systems, e.g., memristors. This is greatly due to diversity and complexity of the subject matter. Thus, we expect a gradual maturation of the field. This includes a deeper penetration into the nanoscale, more control with nano-fabrication techniques, better spatial resolution, and specialization of experimental methods as applied to particular materials. We also expect quantization and a better control of tip-related measurements of CDW conductivity. On the theoretical side, we hope to see specialization of the ab initio theory as applied to the actual charge screening mechanisms, an analysis of the impact of the quantum structure of CDWs on the 2D conductivity, and account for the effect of the wall roughness on the carrier mobility. Involvement of light into various CDW properties also looks highly promising. The fundamental differences between the properties of CDWs and NDWs will be clarified.

As for future applications of CDWs, the general trend here is indeed in miniaturization of the tip-related CDW configurations. Along this way, prototypes of novel reconfigurable functional elements, such as field and stress controlled memory cells, logical elements, and data storage devices, are anticipated. Switch from two- to three-terminal prototypes and fabrication of array structures are also envisaged. Performance of these devices, including such issues as low switching energy, high electrical tunability, memristive functionality, scaling behavior, speed, and endurance and retention characteristics will be considered and improved.

ACKNOWLEDGEMENTS

We are indebted to John Mangeri for numerous comments essentially contributing to the improvement of the manuscript. Jiří Hlinka is acknowledged for reading the manuscript and useful remarks. P.V.Y. acknowledges support from the Institute of Physics of the Czech Academy of Sciences, grant of MSM CR, No. L01409, and from the Institute of Thermophysics SB RAS, grant RSF No. 16-19-00119. P.S.B. and P.V.Y. acknowledge the Operational Program Research, Development and Education financed by European Structural and Investment Funds and the Czech Ministry of Education, Youth and Sports (Project No. SOLID21 - CZ.02.1.01/0.0/0.0/16_019/0000760).

AUTHOR CONTRIBUTIONS

A.K.T. conceived and supervised the project. All authors contributed to the development and discussions of the ideas presented in the paper. P.V.Y., P.S.B., B.I. S., and T.S. were responsible for writing of separate parts of the manuscript. All authors revised and approved the final version of the manuscript.

ADDITIONAL INFORMATION

Supplementary information accompanies the paper on the *npj Computational Materials* website (<https://doi.org/10.1038/s41524-018-0121-8>).

Competing interests: The authors declare no competing interests.

Publisher's note: Springer Nature remains neutral with regard to jurisdictional claims in published maps and institutional affiliations.

REFERENCES

1. Strukov, B. & Levanyuk, A. *Ferroelectric Phenomena in Crystals: Physical Foundations* (Springer, 1998).
2. Jona, F. & Shirane, G. *Ferroelectric Crystals. International Series of Monographs on Solid State Physics* (Pergamon Press, 1962).
3. Tagantsev, A., Cross, L. & Fousek, J. *Domains in Ferroic Crystals and Thin Films* (Springer, 2010).
4. Catalan, G., Seidel, J., Ramesh, R. & Scott, J. F. Domain wall nanoelectronics. *Rev. Mod. Phys.* **84**, 119–156 (2012).
5. Vul, B. M., Guro, G. M. & Ivanchik, I. Encountering domains in ferroelectrics. *Ferroelectrics* **6**, 29–31 (1973).
6. Werner, C. S. et al. Large and accessible conductivity of charged domain walls in lithium niobate. *Sci. Rep.* **7**, 9862 (2017).
7. Sharma, P. et al. Nonvolatile ferroelectric domain wall memory. *Sci. Adv.* **3**, e1700512 (2017).
8. Li, L. et al. Giant resistive switching via control of ferroelectric charged domain walls. *Adv. Mater.* **28**, 6574–6580 (2016).
9. Vasudevan, R. K. et al. Domain wall geometry controls conduction in ferroelectrics. *Nano Lett.* **12**, 5524–5531 (2012).
10. Meier, D. Functional domain walls in multiferroics. *J. Phys. Condens. Matter* **27**, 463003 (2015).
11. Sluka, T., Bednyakov, P., Yudin, P., Crassous, A. & Tagantsev, A. Topological structures in ferroic materials: domain walls, vortices and skyrmions, chap. Charged domain walls in ferroelectrics, 103–138 (Springer International Publishing, 2016).
12. Levanyuk, A. P. & Sannikov, D. G. Improper ferroelectrics. *Sov. Phys. Uspekhi.* **17**, 199 (1974).
13. Bednyakov, P. S., Sluka, T., Tagantsev, A. K., Damjanovic, D. & Setter, N. Formation of charged ferroelectric domain walls with controlled periodicity. *Sci. Rep.* **5**, 15819 (2015).
14. Garrity, K. F., Rabe, K. M. & Vanderbilt, D. Hyperferroelectrics: proper ferroelectrics with persistent polarization. *Phys. Rev. Lett.* **112**, 127601 (2014).
15. Li, P., Ren, X., Guo, G. & He, L. The origin of hyperferroelectricity in LiBO₃ ($B = V, Nb, Ta, Os$). *Sci. Rep.* **6**, 34085 (2016).
16. Liu, S. & Cohen, R. Stable charged antiparallel domain walls in hyperferroelectrics. *J. Phys.: Condens. Matter* **29**, 244003 (2017).
17. Darinskii, B. & Fedosov, V. Structure of 90° domain walls in BaTiO₃. *Sov. Phys. Solid State, Ussr.* **13**, 17–20 (1971).
18. Hlinka, J. & Marton, P. Phenomenological model of a 90° domain wall in BaTiO₃-type ferroelectrics. *Phys. Rev. B.* **74**, 104104 (2006).
19. Fousek, J. & Janovec, V. The orientation of domain walls in twinned ferroelectric crystals. *J. Appl. Phys.* **40**, 135–142 (1969).
20. Grekov, A. A., Adonin, A. A. & Protsenko, N. P. Encountering domains in SbSI. *Ferroelectrics* **13**, 483–485 (1976).
21. Surowiak, Z. et al. Domain-structure formation at phase-transitions. *Ferroelectrics* **20**, 277–279 (1978).
22. Randall, C. A., Barber, D. J. & Whatmore, R. W. Ferroelectric domain configurations in a modified-PZT ceramic. *J. Mater. Sci.* **22**, 925–931 (1987).
23. Shur, V. Y., Rumyantsev, E. L. & Subbotin, A. L. Forming of the domain structure in lead germanate during phase transition. *Ferroelectrics* **140**, 305–312 (1993).
24. Lang, S. B., Kugel, V. D. & Rosenman, G. Direct observation of domain inversion in heat-treated LiNbO₃ using surface laser intensity modulation method. *Ferroelectrics* **157**, 69–74 (1994).
25. Hwang, H. Y. et al. Emergent phenomena at oxide interfaces. *Nat. Mater.* **11**, 103–113 (2012).
26. Lin, P. J. & Bursill, L. A. On the width of charged {110} ferroelectric domain walls in potassium niobate. *Philos. Mag. A* **48**, 251–263 (1983).
27. Gonnissen, J. et al. Direct observation of ferroelectric domain walls in LiNbO₃: wall-meanders, kinks, and local electric charges. *Adv. Funct. Mater.* **26**, 7599–7604 (2016).
28. Matsumoto, T. et al. Multivariate statistical characterization of charged and uncharged domain walls in multiferroic hexagonal YMnO₃ single crystal visualized by a spherical aberration-corrected STEM. *Nano Lett.* **13**, 4594–4601 (2013).
29. Kurushima, K., Yoshimoto, W., Ishii, Y., Cheong, S.-W. & Mori, S. Direct observation of charged domain walls in hybrid improper ferroelectric (Ca,Sr)₃Ti₂O₇. *Jpn. J. Appl. Phys.* **56**, 10PB02 (2017).
30. Lee, M. H. et al. Hidden antipolar order parameter and entangled Néel-type charged domain walls in hybrid improper ferroelectrics. *Phys. Rev. Lett.* **119**, 157601 (2017).
31. Qi, Y. et al. Coexistence of ferroelectric vortex domains and charged domain walls in epitaxial BiFeO₃ film on (110)_o GdScO₃ substrate. *J. Appl. Phys.* **111**, 104117 (2012).
32. Li, L. et al. Atomic scale structure changes induced by charged domain walls in ferroelectric materials. *Nano Lett.* **13**, 5218–5223 (2013).
33. Wang, W.-Y. et al. Atomic level 1D structural modulations at the negatively charged domain walls in BiFeO₃ films. *Adv. Mater. Interfaces* **2**, 1500024–n/a (2015).
34. Tang, Y. L. et al. Atomic-scale mapping of dipole frustration at 90 degrees charged domain walls in ferroelectric PbTiO₃ films. *Sci. Rep.* **4**, 4115 (2014).
35. Jia, C. L. et al. Atomic-scale study of electric dipoles near charged and uncharged domain walls in ferroelectric films. *Nat. Mater.* **7**, 57–61 (2008).
36. Gao, P. et al. Revealing the role of defects in ferroelectric switching with atomic resolution. *Nat. Commun.* **2**, 591 (2011).
37. Gao, P. et al. Atomic-scale mechanisms of ferroelastic domain-wall-mediated ferroelectric switching. *Nat. Commun.* **4**, 2791 (2013).
38. Stolichnov, I. et al. Bent ferroelectric domain walls as reconfigurable metallic-like channels. *Nano Lett.* **15**, 8049–8055 (2015).
39. Han, M.-G. et al. Coupling of bias-induced crystallographic shear planes with charged domain walls in ferroelectric oxide thin films. *Phys. Rev. B.* **94**, 100101 (2016).
40. Wei, X.-K. et al. Controlled charging of ferroelastic domain walls in oxide ferroelectrics. *ACS Appl. Mater. Interfaces* **9**, 6539–6546 (2017).
41. Rojac, T. et al. Domain-wall conduction in ferroelectric BiFeO₃ controlled by accumulation of charged defects. *Sci. Rep.* **16**, 322 (2017).
42. Esin, A. A. et al. Dielectric relaxation and charged domain walls in (K,Na)NbO₃-based ferroelectric ceramics. *J. Appl. Phys.* **121**, 074101 (2017).
43. Zhang, Q. H. et al. Direct observation of interlocked domain walls in hexagonal RMnO₃ ($R = Tm, Lu$). *Phys. Rev. B.* **85**, 020102 (2012).
44. Kokhanchik, L. The use of surface charging in the SEM for lithium niobate domain structure investigation. *Micron* **40**, 41–45 (2009).
45. Schaab, J. et al. Imaging and characterization of conducting ferroelectric domain walls by photoemission electron microscopy. *Appl. Phys. Lett.* **104**, 232904 (2014).
46. Nataf, G. F. et al. Low energy electron imaging of domains and domain walls in magnesium-doped lithium niobate. *Sci. Rep.* **6**, 33098 (2016).
47. Seidel, J. et al. Conduction at domain walls in oxide multiferroics. *Nat. Mater.* **8**, 229–234 (2009).
48. Crassous, A., Sluka, T., Tagantsev, A. K. & Setter, N. Polarization charge as a reconfigurable quasi-dopant in ferroelectric thin films. *Nat. Nanotechnol.* **10**, 614 (2015).
49. Guyonnet, J., Gaponenko, I., Gariglio, S. & Paruch, P. Conduction at domain walls in insulating Pb(Zr_{0.2}Ti_{0.8})O₃ thin films. *Adv. Mater.* **23**, 5377–5382 (2011).
50. Maksymovych, P. et al. Tunable metallic conductance in ferroelectric nanodomains. *Nano Lett.* **12**, 209–213 (2011).
51. Balke, N. et al. Direct observation of capacitor switching using planar electrodes. *Adv. Funct. Mater.* **20**, 3466–3475 (2010).
52. Feigl, L. et al. Controlled creation and displacement of charged domain walls in ferroelectric thin films. *Sci. Rep.* **6**, 31323 (2016).

53. Meier, D. et al. Anisotropic conductance at improper ferroelectric domain walls. *Nat. Mater.* **11**, 284 (2012).
54. Holstad, T. S. et al. Electronic bulk and domain wall properties in B-site doped hexagonal ErMnO_3 . *Phys. Rev. B* **97**, 085143 (2018).
55. Schröder, M. et al. Conducting domain walls in lithium niobate single crystals. *Adv. Funct. Mater.* **22**, 3936–3944 (2012).
56. Shur, V. Y. et al. Formation of self-organized domain structures with charged domain walls in lithium niobate with surface layer modified by proton exchange. *J. Appl. Phys.* **121**, 104101 (2017).
57. Wu, W., Horibe, Y., Lee, N., Cheong, S.-W. & Guest, J. R. Conduction of topologically protected charged ferroelectric domain walls. *Phys. Rev. Lett.* **108**, 077203 (2012).
58. Campbell, M. P. et al. Hall effect in charged conducting ferroelectric domain walls. *Nat. Commun.* **7**, 13764 (2016).
59. McQuaid, R. G. P., Campbell, M. P., Whatmore, R. W., Kumar, A. & Gregg, J. M. Injection and controlled motion of conducting domain walls in improper ferroelectric Cu-Cl boracite. *Nat. Commun.* **8**, 15105 (2017).
60. Oh, Y. S., Luo, X., Huang, F.-T., Wang, Y. & Cheong, S.-W. Experimental demonstration of hybrid improper ferroelectricity and the presence of abundant charged walls in $(\text{Ca,Sr})_2\text{Ti}_2\text{O}_7$ crystals. *Nat. Mater.* **14**, 407 (2015).
61. Kagawa, F. et al. Polarization switching ability dependent on multidomain topology in a uniaxial organic ferroelectric. *Nano Lett.* **14**, 239–243 (2014).
62. Ma, E. Y. et al. Charge-order domain walls with enhanced conductivity in a layered manganite. *Nat. Commun.* **6**, 7595 (2015).
63. Miyazawa, S. Ferroelectric domain inversion in Ti-diffused LiNbO_3 optical waveguide. *J. Appl. Phys.* **50**, 4599–4603 (1979).
64. Nakamura, K., Ando, H. & Shimizu, H. Ferroelectric domain inversion caused in LiNbO_3 plates by heat treatment. *Appl. Phys. Lett.* **50**, 1413–1414 (1987).
65. Shur, V. Y., Romyantsev, E. L., Nikolaeva, E. V. & Shishkin, E. I. Formation and evolution of charged domain walls in congruent lithium niobate. *Appl. Phys. Lett.* **77**, 3636–3638 (2000).
66. Shur, V. Y., Baturin, I. S., Akhmatkhanov, A. R., Chezganov, D. S. & Esin, A. A. Time-dependent conduction current in lithium niobate crystals with charged domain walls. *Appl. Phys. Lett.* **103**, 102905 (2013).
67. Shur, V. Y., Gruverman, A. L., Letuchev, V. V., Romyantsev, E. L. & Subbotin, A. L. Domain structure of lead germanate. *Ferroelectrics* **98**, 29–49 (1989).
68. Sluka, T., Tagantsev, A. K., Bednyakov, P. & Setter, N. Free-electron gas at charged domain walls in insulating BaTiO_3 . *Nat. Commun.* **4**, 1808 (2013).
69. Wada, S., Yako, K., Kakemoto, H., Tsurumi, T. & Kiguchi, T. Enhanced piezoelectric properties of barium titanate single crystals with different engineered-domain sizes. *J. Appl. Phys.* **98**, 014109 (2005).
70. Wada, S., Yako, K., Yokoo, K., Kakemoto, H. & Tsurumi, T. Domain wall engineering in barium titanate single crystals for enhanced piezoelectric properties. *Ferroelectrics* **334**, 293–303 (2006).
71. Wada, S. et al. Domain wall engineering in lead-free piezoelectric crystals. *Ferroelectrics* **355**, 37–49 (2007).
72. Bednyakov, P., Sluka, T., Tagantsev, A., Damjanovic, D. & Setter, N. Free-carrier-compensated charged domain walls produced with super-bandgap illumination in insulating ferroelectrics. *Adv. Mater.* **28**, 9498–9503 (2016).
73. Grabar, A. A., Kedyk, I. V., Stoiak, I. M. & Vysochanskii, Y. M. Reflection of light by charged domain walls in $\text{Sn}_2\text{P}_2\text{S}_6$ uniaxial ferroelectrics. *Ferroelectrics* **254**, 285–293 (2001).
74. Itoh, H., Tokunaga, Y., Kida, N., Shimano, R. & Tokura, Y. Charge-ordering-induced polar domains and domain walls in a bilayered manganite $\text{Pr}(\text{Sr}_{0.15}\text{Ca}_{0.85})_2\text{Mn}_2\text{O}_7$. *Appl. Phys. Lett.* **96**, 032902 (2010).
75. Kämpfe, T. et al. Optical three-dimensional profiling of charged domain walls in ferroelectrics by Cherenkov second-harmonic generation. *Phys. Rev. B* **89**, 035314 (2014).
76. Godau, C., Kämpfe, T., Thiessen, A., Eng, L. M. & Haußmann, A. Enhancing the domain wall conductivity in lithium niobate single crystals. *ACS Nano* **11**, 4816–4824 (2017).
77. Shur, V. Y. et al. Investigation of the nanodomain structure formation by piezoelectric force microscopy and Raman confocal microscopy in LiNbO_3 and LiTaO_3 crystals. *J. Appl. Phys.* **110**, 052013 (2011).
78. Shur, V. Y. & Zelenovskiy, P. S. Micro- and nanodomain imaging in uniaxial ferroelectrics: Joint application of optical, confocal Raman, and piezoelectric force microscopy. *J. Appl. Phys.* **116**, 066802 (2014).
79. Rubio-Marcos, F. et al. Experimental evidence of charged domain walls in lead-free ferroelectric ceramics: light-driven nanodomain switching. *Nanoscale* **10**, 705–715 (2018).
80. Gureev, M. Y., Tagantsev, A. K. & Setter, N. Head-to-head and tail-to-tail 180 degrees domain walls in an isolated ferroelectric. *Phys. Rev. B* **83**, 184104 (2011).
81. Kittel, C. & McEuen, P. *Introduction to Solid State Physics*, 8 (Wiley New York, 1996).
82. Landau, L. D., Lifshitz, E. M. & Pitaevskii, L. *Statistical Physics, Part I* (Pergamon, Oxford, 1980).
83. Tagantsev, A., Shapovalov, K. & Yudin, P. Thick domain walls in non-magnetic ferroics. *Ferroelectrics* **503**, 163–179 (2016).
84. Eliseev, E. A., Morozovska, A. N., Svechnikov, G. S., Gopalan, V. & Shur, V. Y. Static conductivity of charged domain walls in uniaxial ferroelectric semiconductors. *Phys. Rev. B* **83**, 235313 (2011).
85. Landau, L. D. & Lifshitz, E. M. *Quantum Mechanics: Non-relativistic Theory*, 3 (Elsevier, 2013).
86. Yudin, P. V., Gureev, M. Y., Sluka, T., Tagantsev, A. K. & Setter, N. Anomalously thick domain walls in ferroelectrics. *Phys. Rev. B* **91**, 060102 (2015).
87. Sturman, B., Podivilov, E., Stepanov, M., Tagantsev, A. & Setter, N. Quantum properties of charged ferroelectric domain walls. *Phys. Rev. B* **92**, 214112 (2015).
88. Günter, P. & Huignard, J.-P. *Photorefractive Materials and Their Applications*, 1 (Springer, 2006).
89. Sturman, B. & Podivilov, E. Ion and mixed electron-ion screening of charged domain walls in ferroelectrics. *EuroPhys. Lett.* **122**, 67005 (2018).
90. Sturman, B. & Podivilov, E. Charged domain walls under super-band-gap illumination. *Phys. Rev. B* **95**, 104102 (2017).
91. Sze, S. & Ng, K. *Physics of Semiconductor Devices* (John Wiley & Sons, 2006).
92. Holtz, M. E. et al. Topological defects in hexagonal manganites: Inner structure and emergent electrostatics. *Nano Lett.* **17**, 5883–5890 (2017).
93. Artyukhin, S. & Delaney, K. T. & Spaldin, N. A. & Mostovoy, M. Landau theory of topological defects in multiferroic hexagonal manganites. *Nat. Mater.* **13**, 42 (2014).
94. Meyer, B. & Vanderbilt, D. Ab initio study of ferroelectric domain walls in PbTiO_3 . *Phys. Rev. B* **65**, 104111 (2002).
95. Lubk, A., Gemming, S. & Spaldin, N. First-principles study of ferroelectric domain walls in multiferroic bismuth ferrite. *Phys. Rev. B* **80**, 104110 (2009).
96. Liu, S. et al. Ferroelectric domain wall induced band-gap reduction and charge separation in organometal halide perovskites. *J. Phys. Chem. Lett.* **6**, 693–699 (2015).
97. Morozovska, A. Domain wall conduction in ferroelectrics. *Ferroelectrics* **438**, 3–19 (2012).
98. Vasudevan, R. K. et al. Domain wall conduction and polarization-mediated transport in ferroelectrics. *Adv. Funct. Mater.* **23**, 2592–2616 (2013).
99. Volk, T. R., Gainutdinov, R. V. & Zhang, H. H. Domain-wall conduction in AFM-written domain patterns in ion-sliced LiNbO_3 films. *Appl. Phys. Lett.* **110**, 132905 (2017).
100. Mundy, J. A. et al. Functional electronic inversion layers at ferroelectric domain walls. *Nat. Mater.* **16**, 622 (2017).
101. Hlinka, J., Ondrejčević, P. & Marton, P. The piezoelectric response of nanotwinned BaTiO_3 . *Nanotechnology* **20**, 105709 (2009).
102. Balke, N. et al. Deterministic control of ferroelastic switching in multiferroic materials. *Nat. Nanotechnol.* **4**, 868–875 (2009).
103. Wong, K.-K. *Properties of Lithium Niobate*, 28 (IET, 2002).
104. Mohageg, M. et al. Calligraphic poling of lithium niobate. *Opt. Express* **13**, 3408–3419 (2005).
105. Terabe, K. et al. Microscale to nanoscale ferroelectric domain and surface engineering of a near-stoichiometric LiNbO_3 crystal. *Appl. Phys. Lett.* **82**, 433–435 (2003).
106. Kugel, V. D. & Rosenman, G. Domain inversion in heat-treated LiNbO_3 crystals. *Appl. Phys. Lett.* **62**, 2902–2904 (1993).
107. Sones, C. et al. Precision nanoscale domain engineering of lithium niobate via UV laser induced inhibition of poling. *Appl. Phys. Lett.* **92**, 072905 (2008).
108. Johann, F. et al. Depth resolution of piezoresponse force microscopy. *Appl. Phys. Lett.* **94**, 172904 (2009).
109. Steigerwald, H. et al. Origin of UV-induced poling inhibition in lithium niobate crystals. *Phys. Rev. B* **82**, 214105 (2010).
110. Boes, A. et al. Ultraviolet laser-induced poling inhibition produces bulk domains in MgO-doped lithium niobate crystals. *Appl. Phys. Lett.* **105**, 092904 (2014).
111. Ying, C. Y. et al. Light-mediated ferroelectric domain engineering and microstructuring of lithium niobate crystals. *Laser Photonics Rev.* **6**, 526–548 (2012).
112. Sluka, T. & Tagantsev, A. Electronic elements based on quasi two-dimensional electron/hole gas at charged domain walls in ferroelectrics. US Patent 9171602 B2 (2015).
113. Ruff, E. et al. Conductivity contrast and tunneling charge transport in the vortex-like ferroelectric domain patterns of multiferroic hexagonal YMnO_3 . *Phys. Rev. Lett.* **118**, 036803 (2017).
114. Schaab, J. et al. Optimization of electronic domain-wall properties by aliovalent cation substitution. *Adv. Electron. Mater.* **2**, 1500195 (2016).
115. Vasudevan, R. K. et al. Field enhancement of electronic conductance at ferroelectric domain walls. *Nat. Commun.* **8**, 1318 (2017).

116. Jiang, J. et al. Temporary formation of highly conducting domain walls for non-destructive read-out of ferroelectric domain-wall resistance switching memories. *Nat. Mater.* **17**, 49 (2017).
117. Wolba, B. et al. Resistor network modeling of conductive domain walls in lithium niobate. *Adv. Electron. Mater.* **4**, 1700242 (2018).
118. Xiang, Y., Zhang, R. & Cao, W. Piezoelectric properties of domain engineered barium titanate single crystals with different fractions of domain walls. *J. Appl. Phys.* **106**, 064102 (2009).
119. Ondrejko, P., Marton, P., Guennou, M., Setter, N. & Hlinka, J. Piezoelectric properties of twinned ferroelectric perovskites with head-to-head and tail-to-tail domain walls. *Phys. Rev. B* **88**, 024114 (2013).
120. Sluka, T., Tagantsev, A. K., Damjanovic, D., Gureev, M. & Setter, N. Enhanced electromechanical response of ferroelectrics due to charged domain walls. *Nat. Commun.* **3**, 748 (2012).



Open Access This article is licensed under a Creative Commons Attribution 4.0 International License, which permits use, sharing, adaptation, distribution and reproduction in any medium or format, as long as you give appropriate credit to the original author(s) and the source, provide a link to the Creative Commons license, and indicate if changes were made. The images or other third party material in this article are included in the article's Creative Commons license, unless indicated otherwise in a credit line to the material. If material is not included in the article's Creative Commons license and your intended use is not permitted by statutory regulation or exceeds the permitted use, you will need to obtain permission directly from the copyright holder. To view a copy of this license, visit <http://creativecommons.org/licenses/by/4.0/>.

© The Author(s) 2018